PCCP

ROYAL SOCIETY OF CHEMISTRY

PAPER

View Article Online
View Journal | View Issue



Cite this: *Phys. Chem. Chem. Phys.*, 2022, **24**, 25969

# Tuning thermal and electrical properties of MXenes *via* dehydration†

Litao Yu, ‡[a] Dezhao Huang,‡[a] Xuezi Wang,[b] Wei Yu *[bc] and Yanan Yue*[a]

Received 6th August 2022,
Accepted 2nd October 2022

DOI: 10.1039/d2cp03619c

rsc.li/pccp

Recently, MXenes (a class of two-dimensional transition metal carbides) have attracted great attention in various applications such as humidity sensors, owing to their unique electrical and thermal properties. However, previous studies of MXenes mostly focus on their humidity-sensing characteristics such as the mechanical response, and only few reports on their electrical and thermal response are available. Herein, we present novel transient electrothermal experiments to demonstrate that a transition from a negative to a positive resistance–temperature relationship can take place when the MXene sample becomes fully dehydrated. This surprising and unusual phenomenon was elucidated through non-equilibrium molecular dynamics simulations and attributed to water absorption/desorption onto the chemically active MXene surface. A linear relationship was also found between electrical/thermal properties and environmental humidity, which could be related to water adsorption on the surface of the MXene sensor. We further decomposed the total measured thermal conductivity and found that phonons were the dominant thermal carriers in the MXene sample. The main breakthrough of this work is the discovery of the unusual resistance–temperature relationship, which should be applicable to the design of MXene-based sensors for various applications.



## 1. Introduction

MXenes, a class of novel 2D transition metal carbides/nitrides discovered by Gogotsi,[1] have attracted rapidly increasing interest over the past few decades. Their unique physical/chemical/structural properties[2–5] have stimulated a large number of applications in fields such as nanoelectronics,[6,7] catalysis,[8,9] supercapacitors,[10,11] and sensors.[12,13] The general chemical formula of MXenes is $M_{n+1}X_{n+1}T_x$, where M is a transition metal such as Ti, V, Mo, *etc.*, X is carbon or nitrogen, and T is a terminal functional group such as –OH, –O, and –F.[14,15] Among the above applications, humidity sensors have been paid particular attention owing to the ubiquitous presence of water, which makes them critical in fields ranging from healthcare[16] and agriculture to environmental monitoring.[17] Moreover, the combination of unique humidity sensitivity, large surface area, high electrical conductivity, and thermal stability of MXenes makes them ideal materials for humidity sensors.[18–21] It has been reported that MXene films can exhibit a reversible response to relative humidity (RH) values from 0.1% to 95%,[22] and their viscosity increases during adsorption of water. Razai *et al.*[23] also demonstrated that free-standing MXene files present a tensile strength up to 570 MPa and an electrical conductivity greater than 15 000 S $cm^{-1}$.

MXene materials also exhibit abundant terminal groups on their transition metal surface after HF etching, and their chemically active hydrophilic surface can easily attract water molecules. From a molecular point of view, the MXene surface typically interacts with water through hydrogen bonds,[24] intermolecular interactions,[25] or even chemical bonds.[26] For example, Cai *et al.*[27] have exploited the photosynthesis mechanism and complex structure of natural leaves to prepare a MXCC ink and filtered it using a porous polycarbonate filter membrane to obtain a double-layered humidity sensor, in which the cellulose nanofiber and MXene can associate and dissociate through dynamic hydrogen bonds in response to humidity changes. Zhang *et al.*[28] fabricated a MXene film with a one-side periodic structure to obtain an anisotropic quantum-confined superfluidic system and successfully prepared a fast and reversible humidity-responsive MXene film not incorporating other materials. Cao *et al.*[29] further used MXene/cellulose nanofiber/polydopamine (G-MXCP) nanocomposites that relied on the macroscopic hydrophilicity of the films to deform in response to humidity changes. Due to the easy synthesis and chemically

[a] *School of Power and Mechanical Engineering, Wuhan University, Wuhan, Hubei, 430072, P. R. China. E-mail: yyue@whu.edu.cn*
[b] *School of Environmental and Materials Engineering, College of Engineering, Shanghai Second Polytechnic University, Shanghai 201209, China. E-mail: yuwei@sspu.edu.cn*
[c] *Research Center of Resource Recycling Science and Engineering, Shanghai Polytechnic University, Shanghai 201209, China*

† Electronic supplementary information (ESI) available. See DOI: https://doi.org/10.1039/d2cp03619c

‡ L. Y. and D. H. Contributed equally to this work.

active surfaces, MXene have attracted considerable attention among many functional materials such as metal oxides, polymers and other 2D materials.[30,31] MXene generally have greater conductivity in the plane and its unique surfaces allow water molecules to adsorb and intercalate between different MXene sheets.[32,33] The electrical resistance of the MXene will increase when the water intercalates inside these interlayers during the RH sensing process. Wang *et al.*[34] have investigated the static and dynamic properties of MXene-based humidity sensors, and they found that the greater thickness will let more current flows through the sensitive layer. This will give the MXene-based humidity sensors more capacitance, and temperature rises will make water diffuse more quickly and shorten the reaction response time.

Hence, further studies of the electrical and thermal properties of MXenes and of their performance are needed to establish the relationships between their structure and thermophysical properties as potential humidity sensors. Previous studies have shown that MXene-based humidity sensors can exhibit much faster response and higher mechanical stability, owing to their unique structures and active surfaces.[35–38] Li *et al.*[32] have recently fabricated a humidity sensor based on a $Ti_3C_2/T_iO_2$ composite, which exhibited excellent sensitivity at low RH levels. They employed complex impedance spectroscopy and Schottky junction theory to understand the underlying sensing mechanisms and found that the enhanced sensitivity of the composite in lower-moisture environments originates from the barrier of the $Ti_3C_2/T_iO_2$ Schottky junction. Wang *et al.*[39] proposed a spring-like core-sheath structure combining textile substrates and MXenes as a wearable humidity sensor that could also achieve seamless integration with clothing. An *et al.*[30] reported MXene/polyelectrolyte multilayer films with superior response and recovery times to most humidity sensors. They found that water molecules could intercalate into or deintercalate from the MXenes/polyelectrolyte multilayer, causing its thickness to change and producing a rapid response.

Although MXenes are widely known to be suitable materials for humidity sensors, the effects of humidity and temperature on their thermal/electrical properties and the water adsorption/desorption process are still unclear. In this study, a transient electrothermal technique was used to investigate the thermal and electrical response of MXene thin films. Our experimental approach can overcome the long measurement time and low signal limitations of traditional thermophysical techniques and provide accurate and fast results. Nonequilibrium molecular dynamics simulations were also conducted to support our hypothesis and investigate the water evaporation behavior on the MXene surface. A positive relationship between electrical resistance/thermal diffusivity and environmental humidity was found to be related to the water adsorption and desorption on the surface of the MXene sensor. The results of this work may pave the way and provide useful guidelines for the future application of MXene-based humidity sensors.

## 2. Experimental section

### 2.1. Material preparation and characterization

Scanning electron microscopy (SEM) measurements were conducted to inspect the post-etching morphology, post-delamination conditions, and thickness of the samples. Fig. 1a shows the SEM image of the multilayered MXene raw material, exhibiting an accordion-like shape. The MXene monolayers were successfully prepared after sonication; Fig. 1b and c

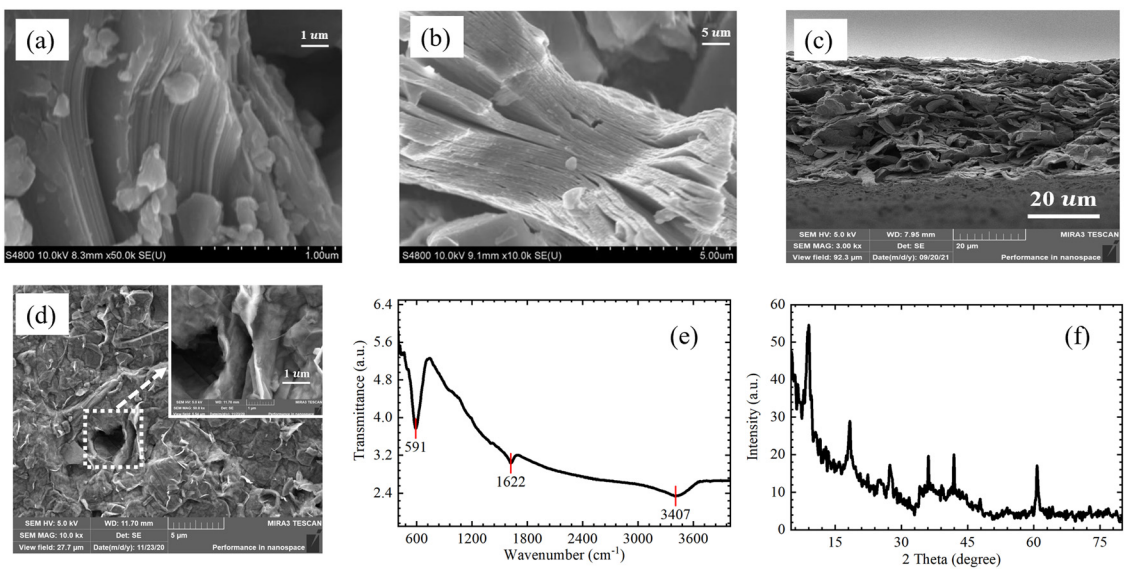


Fig. 1 Morphology characterization of MXene samples. (a) SEM image of layered $Ti_3AlC_2$, displaying an accordion-like shape. (b) SEM image of the multilayered sample. (c) Cross-sectional SEM image of the fabricated sample. (d) SEM image of the porous sample surface. (e) FT-IR spectrum of the multilayered MXene sample. (f) XRD pattern of the multilayered MXene sample. The SEM, FT-IR, and XRD results show that the sensor sample was successfully prepared.

 

show the multilayered and ultrathin morphology of the fabricated MXene sheets. Fig. 1d displays the porous structure of the MXene surface, with an enlarged pore shown in the inset. FT-IR and XRD measurements were conducted to further reveal the structure of the MXene samples.[40–43] The FT-IR spectra were used to further investigate the hydrophilicity of the surface (Fig. 1e). The surface of the MXene samples obtained by etching contained functional groups such as –OH (3407 $cm^{-1}$) and C–F bonds (591 $cm^{-1}$), which reflected its hydrophilic nature. The intense and sharp diffraction peaks shown in Fig. 1f reveal the high purity of the fabricated MXene sample. The (002) diffraction peak was shifted and significantly broadened. Etching reduced the crystallinity of the MXene sample. Furthermore, both XRD and FT-IR results confirm the removal of Al and the successful preparation of the MXene samples.

### 2.2. Experimental details

Due to the large uncertainty of the results of the resistance measurements, a relatively high-precision current source was used to evaluate the resistance of the MXene samples. To avoid changes in the targeted property during the measurement, the step current must be as low as possible. The data collection frequency was set to 1000 Hz to reduce systematic errors. In this work, the thermal diffusivity of the MXene samples was measured using the transient electrothermal technique.[44,45] As shown in Fig. 2a, prior to the measurement, the sample was suspended between two copper electrodes in a vacuum chamber. To ensure a good electrical and thermal contact between the sample and the electrode, silver paste was added to the connection area. When the vacuum reached the steady state, a DC step current was applied to induce Joule heating; thus, the electrical resistance of the sample varied as the temperature changed. The voltage variation of the sample was then recorded to fit the temperature change *vs.* time curve.

Fig. 2b shows a microscopic image (4 × 10 magnification) of the MXene sample standing between the two copper substrates. The sample was made thin and long enough to mimic the one-dimensional heat conduction case. Fig. 2c shows a typical thermophysical measurement profile, in which the transient voltage increase is due to the electrical resistance rise, which originates from the step DC-induced Joule heating. The voltage of the sample increases from an initial value to a final steady-state voltage. The electrical and thermal properties are measured during this transient heating process. The electrical resistance of the sample can be obtained as $R = U(t)/I$; then, the electrical conductivity can be calculated as $\sigma = L/RA$, where $L$ is the sample length, $R$ is the electrical resistance, and $A$ is the cross-sectional area.

During the heating process, the temperature increase of the sample is rather low so that the effect of radiation can be ignored. The governing equation can be written as $\partial \rho c_p T/\partial t = \partial^2 T/\partial x^2 + q_0$, where $\rho$, $c_p$, $k$, and $q_0$ are the density, specific heat, thermal conductivity, and heating power per unit volume, respectively. The copper electrodes used in experiment are much larger than the sample, thus we assumed the temperature of the electrodes maintains constant during the experiment. The initial condition of the physical model is $T(x, t = 0) = T_0$, where $T_0$ indicates room temperature. The boundary conditions are $T(x = 0, t) = T(x = L, t) = T_0$. The average temperature of the sample can be obtained by solving the partial differential equation as:

$$T(t) = T_0 + \frac{8q_0L^2}{k\pi^4}\sum_{m=1}^{\infty}\frac{1-\exp[-(2m-1)^2\pi^2\alpha t/L^2]}{(2m-1)^4} \quad (1)$$

where $\alpha$ refers to the thermal diffusivity of the sample. When the

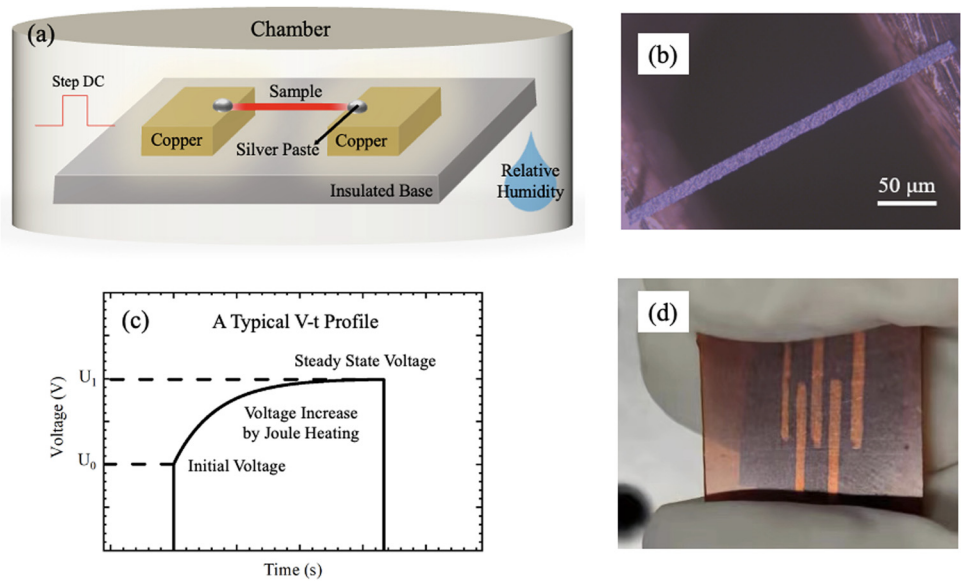


Fig. 2 (a) Schematic illustration of transient electrothermal measurements of thermophysical properties. (b) Photograph of the MXene sample standing between two electrodes, obtained using a 4 × 10 magnification microscope. (c) Typical voltage *vs.* time profile induced by step DC-generated Joule heating in thermophysical measurements. The overall experimental apparatus is placed in a humidity-controlled chamber. (d) Photograph of the fabricated MXene-based humidity sensor.

temperature distribution across the sample reaches the steady state, the final average temperature is $T(t \rightarrow \infty) = T_0 + q_0L^2/12k$. Therefore, the thermal conductivity of the sample can be described as $k = q_0L^2/12\Delta T$. The normalized temperature increase $T^*(t) = [T(t) - T_0]/[T(t \rightarrow \infty) - T_0]$ can then be obtained by solving the partial differential equation as:

$$T^* = \frac{96}{\pi^4}\sum_{m=1}^{\infty}\frac{1-\exp\left[-(2m-1)^2\pi^2\alpha t/L^2\right]}{(2m-1)^4} \quad (2)$$

Because the electrical resistance of the sample is sensitive to the temperature, the normalized temperature can be obtained by calculating the normalized voltage increase, which is defined as $[U(t) - U_0]/[U(t \rightarrow \infty) - U_0]$. Therefore, the thermal diffusivity of the sample can be obtained by a least-squares fit of the voltage profile.

Titanium aluminum carbide ($Ti_3AlC_2$, 400-mesh) was supplied by 11 Technology Co., Ltd.; lithium fluoride (LiF, RG, 99%), hydrofluoric acid (HCl, AR, 36–38%), and L-(+)-ascorbic acid (RG, 99%) were obtained from Shanghai Titan Scientific Co., Ltd. Monolayered MXene was synthesized by mild etching with hydrochloric acid. LiF (1 g) was mixed with 25 mL HCl at room temperature (RT) for 30 min and then stirred. When the reaction was completed, 1 g $Ti_3AlC_2$ was slowly added to the above mixture several times. After the Al elements had been entirely etched out at 55 °C for 36 h, the mixture was washed with deionized water to reach a pH of 6.0. The monolayered MXene suspension was obtained by sonicating the mixture for 3 h under Ar and then centrifuging the supernatant for 1 h. A monolayered MXene nanosheet was then obtained after drying for 24 h. The MXene dispersion was obtained by dispersing 80 mg MXene in 10 mL deionized water. L-(+)-Ascorbic acid (40 mg) was added to the above mixture to enhance the antioxidant capacity of MXene. MXene films were finally obtained by vacuum filtration at room temperature. The fabricated $Ti_3C_2T_x$ thin film was then placed on a polyimide (PI) film to produce the final humidity sensor, as shown in Fig. 2d.

### 2.3. Characterization of thermal properties

The average length and thickness of the MXene samples prepared in this work were 3.026 mm and 42.0 μm, respectively. Because the cross-sectional area values are much smaller than the resistance and length ones, the error associated with thermal conductivity measurements mainly originates from the measurement error of the cross-sectional area.

During the Joule heating cycles, a periodic step DC current with three cycles was applied to the sample to obtain the average voltage profile, which could then be used to estimate the thermal diffusivity value in every measurement. The time interval between subsequent current applications was selected to be long enough to ensure that the temperature of the sample matched that of the environment. The procedure was repeated five times at each temperature, in order to obtain five thermal diffusivity values and reduce the system error. The thermal characterization experiments were conducted from RT to 324.25 K in steps of 3–5 K. It should be noted that the thermal property measurements must be conducted after the temperature of the environment reaches a steady state.

## 3. Results and discussion

### 3.1. Electrical behavior of MXenes before and after dehydration

A step DC was first applied to the sample, and the corresponding voltage varied due to the change in electrical resistance induced by Joule heating. Thermal properties such as conductivity and diffusivity were then extracted from the resulting voltage profile. To investigate the influence of dehydration on the electrical response of the MXene samples, they were tested separately under hydration and dehydration conditions. The black curve in Fig. 3a shows that the voltage of the sample under dehydration conditions first increased and then reached a steady value after 1.6 s. The transient temperature increase was due to the step DC-induced Joule heating, which led to an increase in the electrical resistance of the sample. The overall voltage thus increased; after the temperature of the sample was

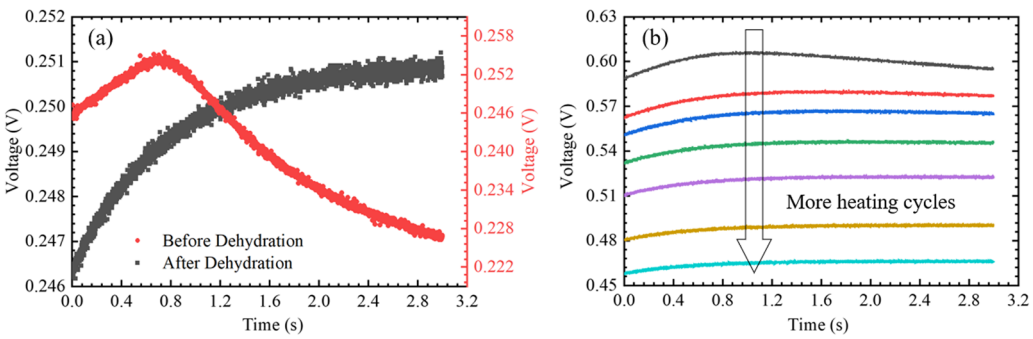


Fig. 3 (a) Voltage profile of samples before (red curve) and after (black curve) dehydration. The sample voltage exhibits an increasing and decreasing trend before the dehydration process, while the dehydrated sample gradually increases to a steady-state value. Due to their initial water contents, the initial voltages of the hydrated and dehydrated samples are also different. (b) Voltage profiles for different heating cycles. Subsequent heating cycles gradually reduce the water content of the sample and the electrical resistance eventually reaches a stable value, finally resulting in a flat voltage profile.

 

stabilized, the resistance of the sample reached a steady state and a flat voltage profile was eventually obtained.

However, the red curve in Fig. 3a clearly shows that the voltage of the sample initially increased and then rapidly dropped to a much lower value than in the hydrated state. This is likely due to the chemically active MXene surface, which adsorbed water molecules from the surrounding environment. During the Joule heating process, the electrical resistance of the sample rapidly increases, before the adsorbed water molecules are released from the surface. After sufficient heating, the water molecules tend to gradually leave the surface of the sample, leading to a decrease in the voltage. To further validate this hypothesis, the MXene samples were subjected to repeated heating cycles to eliminate the influence of the adsorbed water molecules and assess their influence on the electrical resistance behavior. As shown in Fig. 3b, the voltage profile gradually changed under repeated heating cycles. The black and cyan curves display the voltage *vs.* time profiles in the first and last heating cycles, respectively; after a sufficient number of cycles, the voltage profile reached a steady state. This further confirms previous observations that the environmental conditions might influence the electrical properties of MXenes. The generated Joule heating provides enough energy for the absorbed water inside the MXene film to detach, which leads to the resistance decrease. Further heating cycles gradually remove the adsorbed water molecules from the MXene surface, and their influence on the electrical properties becomes negligible. After a sufficient number of heating cycles, the water content adsorbed on the surface is entirely removed, and the sample voltage shows a standard profile in the last heating cycle, reaching a final steady value.

The electrical resistance of the MXene samples decreased linearly as a function of temperature (Fig. 4a), reflecting a negative intrinsic resistance temperature coefficient (RTC) in a vacuum environment. Higher temperatures will lead to a lower electrical resistance because the exfoliated MXene samples are usually etched in HF solutions. Their surface is usually chemically terminated with –O, –OH, and –F functional groups and might easily adsorb the surrounding water molecules from the environment, which affect its electronic transport properties. Higher temperatures might result in the gradual removal of water molecules from the MXene surface and reduce the electrical resistance. The calibration curve of the resistance temperature coefficient after a sufficient number of heating cycles shows the same trend as that displayed in Fig. 4b, which reveals the positive resistance–temperature relationship of the sample. The above observations further confirm that the different (vacuum or ambient) conditions are the reason for the inconsistency between the resistance and voltage variations of the MXene sample.

### 3.2. Thermal diffusivity under repeated heating cycles

To understand the influence of the water content on the thermal diffusivity of the MXene samples, they were subjected to different number of heating cycles. In addition to the electrical properties, we characterized the thermal properties of the samples, as shown in Fig. 5a. The thermal diffusivity rapidly decreased with the number of heating cycles and reached a plateau value of approximately $1.47 \times 10^{-6}$ m$^2$ s$^{-1}$. Further heating cycles gradually removed the adsorbed water molecules from the MXene surface and led to a decrease in the thermal diffusivity value. Each error bar was obtained by calculating the standard deviation of the three independent experiment results. To fully eliminate the effects of moisture on the measured thermal properties and identify the relation between the MXene response and the temperature, the sample was heated to 336 K for 2 h in a vacuum environment before the experiment. Therefore, the moisture of the environment would not affect the measured thermal properties below 336 K. Fig. 5b shows that thermal diffusivity increased linearly with temperature, then remained stable after reaching the steady state, and its final value varied from $1.38 \times 10^{-6}$ to $1.56 \times 10^{-6}$ m$^2$ s$^{-1}$.

### 3.3. Humidity dependence of electrical/thermal properties of MXene thin films

To further understand the role of environmental humidity on the electrical and thermal properties of the MXene samples, we investigated the electrical conductivities and thermal diffusivities under different RH conditions. The environmental humidity range was chosen to be sufficiently wide to test the

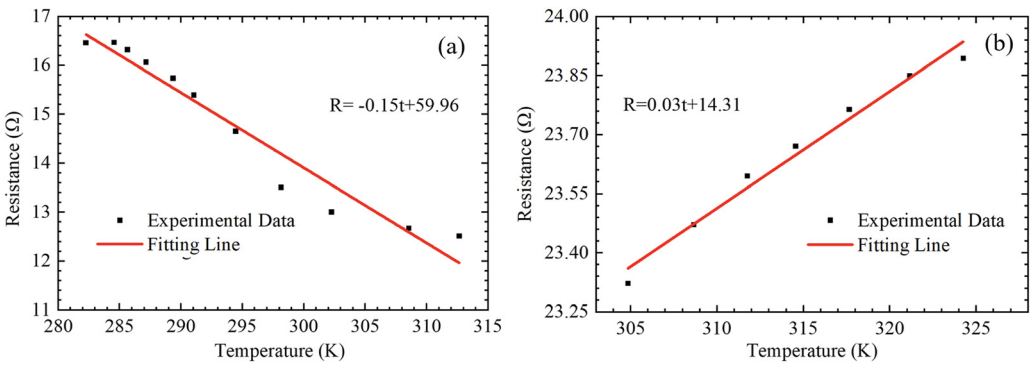


Fig. 4 (a) Electrical resistance–temperature calibration curve before dehydration. Higher temperatures gradually remove the water content from the sample and lead to a lower electrical resistance. (b) Electrical resistance–temperature calibration curve after dehydration. After the full dehydration process, the influence of the water content becomes negligible; thus, the electrical resistance increases with increasing temperature.

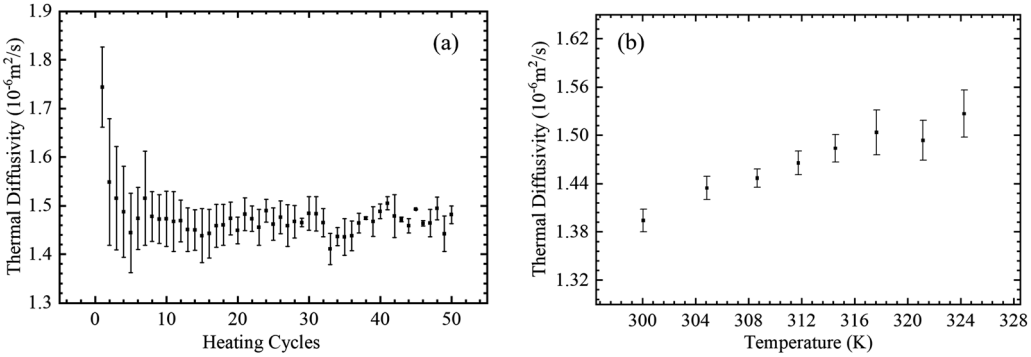


Fig. 5 (a) Thermal diffusivity as a function of number of heating cycles. The thermal diffusivity of the sample shows a rapid decrease and, after a sufficient number of cycles, reaches a steady-state value after the water content is fully removed from the MXene surface. (b) Thermal diffusivity at different temperatures. Higher temperatures lead to a slowly increasing thermal diffusivity, which reaches a plateau above ~316 K.

sensitivity of the electrical properties of the MXene samples to the water content. The RH value is the percentage of water (moisture-holding capacity) that the atmosphere can retain at a given temperature and pressure without condensation. Fig. 6a shows that the electrical conductivity of the MXene samples exhibited a close relationship with the environmental humidity. The electrical conductivity decreased with increasing RH, due to the higher number of adsorbed water molecules on the chemically active sample surface. The electrical conductivity of the MXene samples exhibited a better response in the environmental humidity range between 24% and 80%, which indicates excellent adaptability to the environmental humidity conditions. Fig. 6b illustrates the relationship between thermal diffusivity and RH. The thermal diffusivity increased with a parabolic trend with increasing relative humidity, which confirms the potential of the present samples as humidity sensors.

The analysis of the temperature dependence of the electrical and thermal conductivities of the MXenes samples in Fig. 7a shows that electrical conductivity decreased gradually as the temperature increased, which is consistent with the previous electrical resistance and temperature calibration results. The negative resistance *vs.* temperature relationship changed to a positive intrinsic resistance temperature coefficient after the full dehydration process. The black datapoints in Fig. 7b show that the total thermal conductivity value increased in the range of 300 to 315 K and reached a steady-state plateau above 315 K. The heat carriers can be divided into electrons and phonons according to the Wiedemann–Franz law $L_0 = k_e/\sigma T$, where $L_0$ is the Lorenz number, $k_e$ is the electronic contribution to thermal conductivity, $\sigma$ is the electrical conductivity, and $T$ is the temperature; this enables the calculation of electronic contribution to thermal conductivity. As shown by the red symbols in Fig. 7b, this contribution was approximately $7.2 \times 10^{-2}$ W m$^{-1}$ K$^{-1}$, which represented only ~0.5% of the total thermal conductivity. These results strongly indicate that the dominant heat carriers inside the MXene sample were phonons, rather than electrons.

## 4. Physical interpretation *via* molecular dynamics simulations

### 4.1. Simulation model and methods

To further reveal the molecular mechanism of the MXene response to humidity, we performed molecular dynamics simulations of water evaporation from the MXene surface. In this simulation, the MXene surface was functionalized with three types of terminal groups: –OH, –O, and –F.[15,46,47] For convenience, only –OH functional groups were functionalized on the MXene surface. The expected hydrophilicity is high enough to

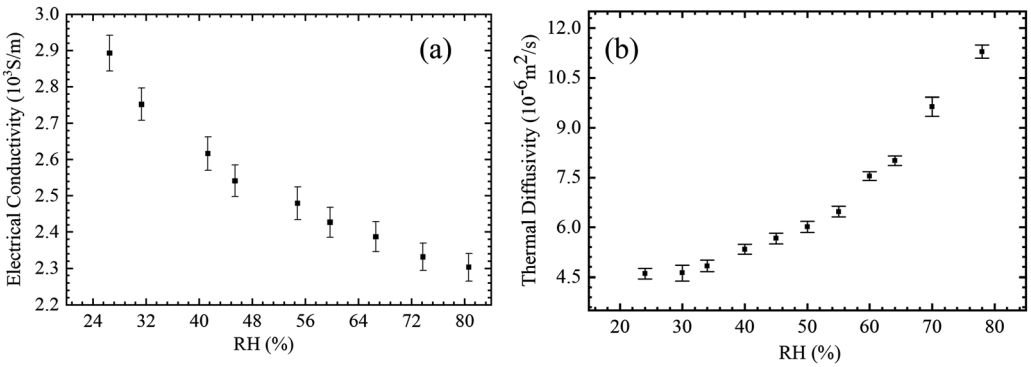


Fig. 6 Effect of relative humidity on (a) electrical conductivity and (b) thermal diffusivity of MXene samples. A higher humidity results in a lower electrical conductivity along with a higher thermal diffusivity, due to the higher number of adsorbed water on the chemically active surface of the sample.

 

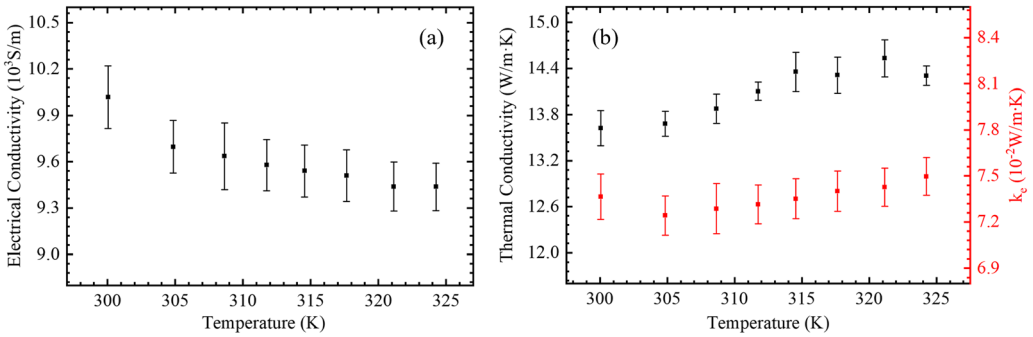


Fig. 7 Temperature dependence of (a) electrical conductivity and (b) thermal conductivity and the corresponding electronic component. The black and red symbols denote the total thermal conductivity and its electronic component, respectively. Higher temperatures lead to gradually lower electrical conductivity and higher thermal conductivity values. The electronic component of the total thermal conductivity is only ~0.5%, which indicates that the main heat carriers inside the sample are phonons, rather than electrons.

represent mixed –OH/–F/–O-functionalized surfaces. Water molecules were modeled using the TIP3P force field,[48] which accurately reproduces the thermodynamic and structural properties of water. The MXene material was modeled using the ClayFF force field, which has been successfully used for structural studies involving MXenes. The nonbonded interactions between MXenes and the other atoms were simulated by the Lennard-Jones (L-J) potential $E = 4\varepsilon[(\sigma/r_{ij})^{12} - (\sigma/r_{ij})^{6}]$, where $\varepsilon$ and $\sigma$ are the representative scales of energy and length, whereas $r_{ij}$ is the distance between $i$ and $j$ molecules. The L-J interaction parameters were extracted from the modified Universal Force Field (UFF).[49] A 10 Å cutoff was chosen for the L-J interactions. Long-range electrostatic interactions in the entire system were calculated using the particle–particle particle–mesh (PPPM) approach, with an accuracy of $1 \times 10^{-15}$.[50,51] The simulations were performed using the large-scale atomic/molecular massively parallel simulator (LAMMPS) program.[52] Nonequilibrium MD (NEMD) simulations were performed to mimic the evaporation process.[53–57] Langevin thermostats were used to control the temperatures in the thermostatted regions; the simulation system was equilibrated in the canonical (NVT) ensemble at 300 K for 2 ns and 370 K for the evaporation process.

### 4.2. Evaporation dynamics

All the experimental observations discussed above reflect the interfacial adsorption/desorption of water molecules on the MXene surface; this interpretation is well supported by the results of our MD simulations. The hydrophilic nature of the –OH, –O, and –F functional groups on the MXene surface promotes water adsorption. The relation between the temperature and the adsorbed water molecules on the surface was

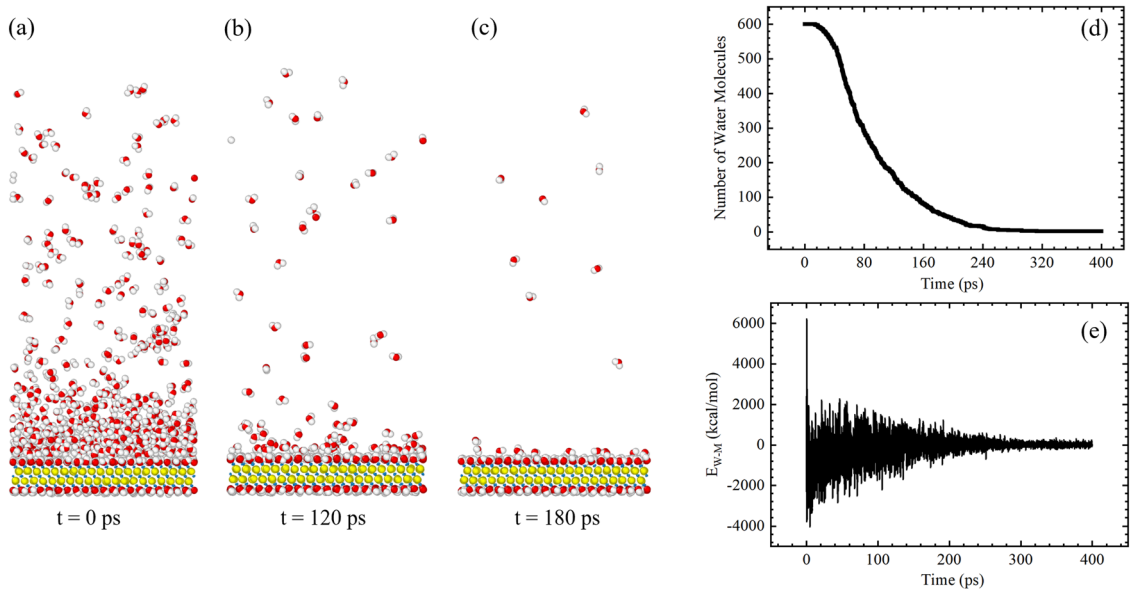


Fig. 8 Molecular dynamics simulations of water evaporation on the MXene surface. The water molecules disappear with increasing simulation time. Snapshots of the system at (a) 0 ps, (b) 120 ps, and (c) 460 ps; (d) number of water molecules left in the system; (e) interaction energy between water molecules and the MXene surface during the evaporation process. The adsorbed water molecules gradually detach from the surface of the MXene substrate due to the higher kinetic energy gained, leading to a lower interaction energy with the surface.

determined by analyzing the detailed water evaporation process, as shown in Fig. 8. The MXene substrate was heated to 370 K to mimic the evaporation process of water molecules. Fig. 8a–c clearly show the disappearance of the water molecules with the simulation time. A lower environmental humidity will result in fewer water molecules adsorbed on the MXene surface and lead to lower electrical resistance, thermal diffusivity, and thermal conductivity values because the water thermal conductivity is $\sim$0.598 W $m^{-1}$ $K^{-1}$ under ambient conditions. We calculated the number of water molecules left in the system as the MXenes surface was heated; as shown in Fig. 8d, the water molecules gradually detached from the surface. The fewer water molecules remaining in the system led to a weaker interaction with the MXenes surface. The interaction energy between water and the MXene surface was calculated by summing up the corresponding electrostatic and van der Waals energies, as shown in Fig. 8e. The interaction energy rapidly decreased at the beginning of the evaporation process and then oscillated around zero until the end of the process, which indicated the absence of interactions between water and the MXene surface.

## 5. Conclusions

In this study, thermal experiments and molecular dynamics simulations were performed to study the electrical and thermal properties of an MXene-based sensor under different RH and temperature conditions. The results of the measurements performed before and after dehydration clearly show that the MXene-based sensor undergoes a transition from a negative to a positive resistance–temperature relationship. Further analysis reveals that phonons (rather than electrons) are the dominant heat carriers in the MXene sample; moreover, the linear relationship between the electrical/thermal properties and the environmental humidity is found to be related to water adsorption/desorption on the sensor surface. Furthermore, the fabricated humidity sensor shows good stability and durability, and its electrical/thermal properties maintain a sensitive and linear response to the humidity conditions. The results of this work are expected to have important implications for understanding the response of MXene-based humidity sensors and for designing effective guidelines to support future applications of these systems.

## Data availability

The data that support the findings of this study are available from the corresponding author upon reasonable request.

## Author contributions

Litao Yu: data curation, investigation, methodology, writing – original draft (equal). Dezhao Huang: data curation, investigation, methodology, funding acquisition, writing – original draft(equal). Xuezi Wang: resources, methodology. Wei Yu: resources, validation. Yanan Yue: formel analysis, funding acquisition, methodology, project administration, supervision.

## Conflicts of interest

There are no conflicts to declare.

## Acknowledgements

This work was supported by the National Key Research and Development Program of China (No. 2019YFE0119900), the National Natural Science Foundation of China (No. 52076156), the Fundamental Research Funds for the Central Universities (No. 2042020kf0194) and China Postdoctoral Science Foundation (No. 2022M712447). The simulations were supported by the Research Computing Center of Wuhan University.

## References

1 M. Naguib, M. Kurtoglu and V. Presser, *et al.*, Two-dimensional nanocrystals produced by exfoliation of ti3alc2, *Adv. Mater.*, 2011, **23**, 4248–4253.
2 H. Shin, W. Eom and K. H. Lee, *et al.*, Highly electroconductive and mechanically strong $Ti_3C_2T_x$ mxene fibers using a deformable mxene gel, *ACS Nano*, 2021, **15**, 3320–3329.
3 T. S. Mathis, K. Maleski and A. Goad, *et al.*, Modified max phase synthesis for environmentally stable and highly conductive $Ti_3C_2$ mxene, *ACS Nano*, 2021, **15**, 6420–6429.
4 H. Alijani, A. R. Rezk and M. M. Khosravi Farsani, *et al.*, Acoustomicrofluidic synthesis of pristine ultrathin $Ti_3C_2TZ$ mxene nanosheets and quantum dots, *ACS Nano*, 2021, **15**, 12099–12108.
5 P. Mayorga Burrezo, J. Muñoz and D. Zaoralová, *et al.*, Multiresponsive 2d $Ti_3C_2T_x$ mxene via implanting molecular properties, *ACS Nano*, 2021, **15**, 10067–10075.
6 D. Akinwande, N. Petrone and J. Hone, Two-dimensional flexible nanoelectronics, *Nat. Commun.*, 2014, **5**, 5678.
7 N. R. Glavin, C. Muratore and M. L. Jespersen, *et al.*, Amorphous boron nitride: A universal, ultrathin dielectric for 2d nanoelectronics, *Adv. Funct. Mater.*, 2016, **26**, 2640–2647.
8 J. Deng, D. Deng and X. Bao, Robust catalysis on 2d materials encapsulating metals: Concept, application, and perspective, *Adv. Mater.*, 2017, **29**, 1606967.
9 T. A. Shifa, F. Wang and Y. Liu, *et al.*, Heterostructures based on 2d materials: A versatile platform for efficient catalysis, *Adv. Mater.*, 2019, **31**, 1804828.
10 Y. Liu and X. Peng, Recent advances of supercapacitors based on two-dimensional materials, *Appl. Mater. Today*, 2017, **8**, 104–115.
11 T. Palaniselvam and J. B. Baek, Graphene based 2d-materials for supercapacitors, *2D Mater.*, 2015, **2**, 032002.

 

12 L. Zhang, K. Khan and J. Zou, *et al.*, Recent advances in emerging 2d material-based gas sensors: Potential in disease diagnosis, *Adv. Mater. Interfaces*, 2019, **6**, 1901329.
13 Y. Cai, J. Shen and G. Ge, *et al.*, Stretchable $Ti_3C_2T_x$ mxene/carbon nanotube composite based strain sensor with ultrahigh sensitivity and tunable sensing range, *ACS Nano*, 2018, **12**, 56–62.
14 L. H. Karlsson, J. Birch and J. Halim, *et al.*, Atomically resolved structural and chemical investigation of single mxene sheets, *Nano Lett.*, 2015, **15**, 4955–4960.
15 P. Zandi, E. Ghasemy and M. Khedri, *et al.*, Shedding light on miniaturized dialysis using mxene 2d materials: A computational chemistry approach, *ACS Omega*, 2021, **6**, 6312–6325.
16 Y. T. Jao, P. K. Yang and C. M. Chiu, *et al.*, A textile-based triboelectric nanogenerator with humidity-resistant output characteristic and its applications in self-powered healthcare sensors, *Nano Energy*, 2018, **50**, 513–520.
17 J. Paek, J. Hicks and S. Coe, *et al.*, Image-based environmental monitoring sensor application using an embedded wireless sensor network, *Sensors*, 2014, **14**, 15981–16002.
18 T. Yun, H. Kim and A. Iqbal, *et al.*, Electromagnetic shielding of monolayer mxene assemblies, *Adv. Mater.*, 2020, **32**, 1906769.
19 X. Zhao, L. Y. Wang and C. Y. Tang, *et al.*, Smart $Ti_3C_2T_x$ mxene fabric with fast humidity response and joule heating for healthcare and medical therapy applications, *ACS Nano*, 2020, **14**, 8793–8805.
20 S. Célérier, S. Hurand and C. Garnero, *et al.*, Hydration of $Ti_3C_2T_x$ mxene: An interstratification process with major implications on physical properties, *Chem. Mater.*, 2019, **31**, 454–461.
21 Y. Pei, X. Zhang and Z. Hui, *et al.*, $Ti_3C_2T_x$ mxene for sensing applications: Recent progress, design principles, and future perspectives, *ACS Nano*, 2021, **15**, 3996–4017.
22 E. S. Muckley, M. Naguib and I. N. Multi-modal Ivanov, Ultrasensitive, wide-range humidity sensing with $Ti_3C_2$ film, *Nanoscale*, 2018, **10**, 21689–21695.
23 J. Zhang, N. Kong and S. Uzun, *et al.*, Scalable manufacturing of free-standing, strong $Ti_3C_2T_x$ mxene films with outstanding conductivity, *Adv. Mater.*, 2020, **32**, 2001093.
24 J. Wu, P. Lu and J. Dai, *et al.*, High performance humidity sensing property of $Ti_3C_2T_x$ mxene-derived $Ti_3C_2T_x/K_2TI_4O_9$ composites, *Sens. Actuators, B*, 2021, **326**, 128969.
25 H. Liao, X. Guo and P. Wan, *et al.*, Conductive mxene nanocomposite organohydrogel for flexible, healable, low-temperature tolerant strain sensors, *Adv. Funct. Mater.*, 2019, **29**, 1904507.
26 H. Riazi, G. Taghizadeh and M. Soroush, Mxene-based nanocomposite sensors, *ACS Omega*, 2021, **6**, 11103–11112.
27 G. Cai, J. H. Ciou and Y. Liu, *et al.*, Leaf-inspired multiresponsive mxene-based actuator for programmable smart devices, *Sci. Adv.*, 2019, **5**, eaaw7956.
28 Y. L. Zhang, Y. Q. Liu and D. D. Han, *et al.*, Quantum-confined-superfluidics-enabled moisture actuation based on unilaterally structured graphene oxide papers, *Adv. Mater.*, 2019, **31**, 1901585.
29 J. Cao, Z. Zhou and Q. Song, *et al.*, Ultrarobust $Ti_3C_2T_x$ mxene-based soft actuators via bamboo-inspired mesoscale assembly of hybrid nanostructures, *ACS Nano*, 2020, **14**, 7055–7065.
30 H. An, T. Habib and S. Shah, *et al.*, Water sorption in mxene/polyelectrolyte multilayers for ultrafast humidity sensing, *ACS Appl. Nano Mater.*, 2019, **2**, 948–955.
31 Z. Yang, A. Liu and C. Wang, *et al.*, Improvement of gas and humidity sensing properties of organ-like mxene by alkaline treatment, *ACS Sens.*, 2019, **4**, 1261–1269.
32 N. Li, Y. Jiang and C. Zhou, *et al.*, High-performance humidity sensor based on urchin-like composite of $Ti_3C_2$ mxene-derived $TiO_2$ nanowires, *ACS Appl. Mater. Interfaces*, 2019, **11**, 38116–38125.
33 G. Jia, A. Zheng and X. Wang, *et al.*, Flexible, biocompatible and highly conductive mxene-graphene oxide film for smart actuator and humidity sensor, *Sens. Actuators, B*, 2021, **346**, 130507.
34 Y. Wang, C. Hu and Z. Li, *et al.*, Theoretical and simulation analysis of static and dynamic properties of mxene-based humidity sensors, *Appl. Sci.*, 2022, **12**, 8254.
35 Z. Yang, A. Liu and C. Wang, *et al.*, Improvement of gas and humidity sensing properties of organ-like mxene by alkaline treatment, *ACS Sens.*, 2019, **4**, 1261–1269.
36 D. Wang, D. Zhang and P. Li, *et al.*, Electrospinning of flexible poly(vinyl alcohol)/mxene nanofiber-based humidity sensor self-powered by monolayer molybdenum diselenide piezoelectric nanogenerator, *Nano-Micro Lett.*, 2021, **13**, 57.
37 G. Song, R. Kang and L. Guo, *et al.*, Highly flexible few-layer $Ti_3C_2$ mxene/cellulose nanofiber heat-spreader films with enhanced thermal conductivity, *New J. Chem.*, 2020, **44**, 7186–7193.
38 L. X. Liu, W. Chen and H. B. Zhang, *et al.*, Flexible and multifunctional silk textiles with biomimetic leaf-like mxene/silver nanowire nanostructures for electromagnetic interference shielding, humidity monitoring, and self-derived hydrophobicity, *Adv. Funct. Mater.*, 2019, **29**, 1905197.
39 L. Wang, M. Tian and Y. Zhang, *et al.*, Helical core-sheath elastic yarn-based dual strain/humidity sensors with mxene sensing layer, *J. Mater. Sci.*, 2020, **55**, 6187–6194.
40 M. Volkov, E. Willinger and D. A. Kuznetsov, *et al.*, Photoswitchable nanoripples in $Ti_3C_2T_x$ mxene, *ACS Nano*, 2021, **15**, 14071–14079.
41 D. Kim, T. Y. Ko and H. Kim, *et al.*, Nonpolar organic dispersion of 2d $Ti_3C_2T_x$ mxene flakes via simultaneous interfacial chemical grafting and phase transfer method, *ACS Nano*, 2019, **13**, 13818–13828.
42 J. H. Kim, G. S. Park and Y. J. Kim, *et al.*, Large-area $Ti_3C_2T_x$-mxene coating: Toward industrial-scale fabrication and molecular separation, *ACS Nano*, 2021, **15**, 8860–8869.
43 H. Jing, H. Yeo and B. Lyu, *et al.*, Modulation of the electronic properties of mxene ($Ti_3C_2T_x$) via surface-covalent functionalization with diazonium, *ACS Nano*, 2021, **15**, 1388–1396.
44 J. Guo, X. Wang and T. Wang, Thermal characterization of microscale conductive and nonconductive wires using

transient electrothermal technique, *J. Appl. Phys.*, 2007, **101**, 063537.

45 X. Feng, X. Huang and X. Wang, Nonlinear effects in transient electrothermal characterization of anatase $TiO_2$ nanowires, *Rev. Sci. Instrum.*, 2012, **83**, 044901.

46 L. Ding, Y. Wei and L. Li, *et al.*, Mxene molecular sieving membranes for highly efficient gas separation, *Nat. Commun.*, 2018, **9**, 155.

47 D. Wu, R. Zhao and Y. Chen, *et al.*, Molecular insights into mxene destructing the cell membrane as a ''nano thermal blade'', *PCCP*, 2021, **23**, 3341–3350.

48 W. L. Jorgensen, J. Chandrasekhar and J. D. Madura, *et al.*, Comparison of simple potential functions for simulating liquid water, *J. Chem. Phys.*, 1983, **79**, 926–935.

49 A. K. Rappe, C. J. Casewit and K. S. Colwell, *et al.*, Uff, a full periodic table force field for molecular mechanics and molecular dynamics simulations, *J. Am. Chem. Soc.*, 1992, **114**, 10024–10035.

50 D. Huang, T. Zhang and G. Xiong, *et al.*, Tuning water slip behavior in nanochannels using self-assembled monolayers, *ACS Appl. Mater. Interfaces*, 2019, **11**, 32481–32488.

51 D. Huang, R. Ma and T. Zhang, *et al.*, Origin of hydrophilic surface functionalization-induced thermal conductance enhancement across solid–water interfaces, *ACS Appl. Mater. Interfaces*, 2018, **10**, 28159–28165.

52 S. Plimpton, Fast parallel algorithms for short-range molecular dynamics, *J. Comput. Phys.*, 1995, **117**, 1–19.

53 Z. Liang, A. Chandra and E. Bird, *et al.*, A molecular dynamics study of transient evaporation and condensation, *Int. J. Heat Mass Transfer*, 2020, **149**, 119152.

54 J. Yu and H. Wang, A molecular dynamics investigation on evaporation of thin liquid films, *Int. J. Heat Mass Transfer*, 2012, **55**, 1218–1225.

55 R. Stierle, C. Waibel and J. Gross, *et al.*, On the selection of boundary conditions for droplet evaporation and condensation at high pressure and temperature conditions from interfacial transport resistivities, *Int. J. Heat Mass Transfer*, 2020, **151**, 119450.

56 G. Nagayama, M. Kawagoe and A. Tokunaga, *et al.*, On the evaporation rate of ultra-thin liquid film at the nanostructured surface: A molecular dynamics study, *Int. J. Therm. Sci.*, 2010, **49**, 59–66.

57 E. Bird and Z. Liang, Transport phenomena in the knudsen layer near an evaporating surface, *Phys. Rev. E*, 2019, **100**, 043108.

 